Fracture toughness of single grains and polycrystalline $Li_7La_3Zr_2O_{12}$ electrolyte material based on a pillar splitting method

Juliane Franciele Nonemacher[1], Yulia Arinicheva[2], Gang Yan[1*], Martin Finsterbusch[2], Manja Krüger[1], Jürgen Malzbender[1†]

[1]Institute for Energy and Climate Research, Microstructure and Properties of Materials (IEK-2), Forschungszentrum Jülich GmbH, 52425 Jülich, Germany

[2]Institute for Energy and Climate Research, Materials Synthesis and Processing (IEK-1), Forschungszentrum Jülich GmbH, 52425 Jülich, Germany

Abstract

In the present study an advanced pillar splitting method is used to determine the fracture toughness of a garnet-type $Li_7La_3Zr_2O_{12}$ (LLZO) electrolyte. The obtained results are compared to data derived on the basis of conventional Vickers indentation. Furthermore, potential micro-pillar size effects are investigated. The estimated fracture toughness values for single grains and polycrystalline LLZO material obtained via both methods are in good agreement, yielding ~ 1 $MPa \cdot m^{0.5}$, hence the data indicate that LLZO exhibits relatively low fracture toughness and has a brittle behavior.

Keywords: Lithium-ion batteries; solid electrolyte; LLZO; fracture toughness; indentation; pillar splitting

---

[*] g.yan@fz-juelich.de; tel: +492461616477.; fax: ++492461613699

[†] j.malzbender@fz-juelich.de; tel: +492461616964.; fax: ++492461613699

1. Introduction

All-solid-state Li-batteries (ASSB) belong to the most promising electrochemical energy storage systems, allowing to overcome safety concerns of the conventional Li-ion batteries due to the lack of flammable organic components and to improve potentially the energy density [1-3]. One of the key components enabling rechargeable ASSB technology is a solid electrolyte. The garnet-type $Li_7La_3Zr_2O_{12}$ (LLZO) is a promising solid-state electrolyte material for future high capacity solid state batteries due to its electrochemical and chemical stability in contact with metallic lithium and high ionic conductivity [4-6].

Supervalent cations doping by e.g. Al^{3+}, Ga^{3+} on Li-sites or Ta^{5+}, Nb^{+5} on Zr-sites [7-11] creates Li vacancies and stabilizes the cubic structure, leading to a more than two orders of magnitude higher conductivity ($\sim 10^{-3} – 10^{-4}$ S cm^{-1} at RT) in comparison to the conductivity of the tetragonal phase ($\sim 10^{-6}$ S cm^{-1} at RT) [7-11]. Besides high ionic conductivity and chemical and electrochemical stability, mechanical stability [15-19] belongs to the important properties of solid electrolytes, significantly influencing the battery manufacturing processes and performance. Thus, with respect to cycling, potential volume expansions of the electrode materials can occur due to rapid Li-ions intercalation inducing significant stresses [20, 21]. This mechanism can eventually cause the formation of micro-cracks within the electrolyte itself and at the electrode/electrolyte interface, hence, reducing the cyclic life and compromising the stability of the entire battery [22-26]. Moreover, nucleation of Li dendrites and its propagation in LLZO electrolyte is reported to be a function of grain boundary resistance and fracture stress of the electrolyte [27, 28].

Therefore the fracture toughness of solid electrolytes is particularly crucial since it represents the resistance to crack growth that might occur during battery operation rendering eventually the device inoperable. The fracture toughness is related to atomic bonding, crystal structure and microstructure and can also be used to estimate the macroscopic fracture stress [29-31].

A number of studies have been dedicated to the mechanical stability of LLZO electrolytes [14, 16, 18, 32-37]. According to the literature the fracture toughness (K_{IC}) of LLZO with nominal composition $Li_{6.19}Al_{0.27}La_3Zr_2O_{12}$ based on Vickers indentation fracture (VIF) varied in a rather wide range from 0.97 to 2.37 $MPa{\cdot}m^{0.5}$ as the relative density decreased from 98% to 85% for an average grain size of ~3 μm , in addition a transition from intragranular to intergranular crack mode was reported [35]. In another study, the K_{IC} of $Li_{6.28}Zr_2La_3Al_{0.24}O_{12}$ with relative density of 97% and grain size of ∼5 μm ranged from 0.86 to 1.63 $MPa{\cdot}m^{0.5}$ when determined from Vickers indentation using different models for calculation, that were required by a transition from half-penny crack shape to Palmqvist type [36]. The effect of grain size on the fracture toughness of LLZO samples with nominal composition $Li_{6.25}Al_{0.25}La_3Zr_2O_{12}$ was investigated by VIF-method [38]. LLZO material with smaller grain size possessed a slightly higher fracture toughness. However, the sample with smaller grains had a 3.4% lower density, which could have had an impact on the fracture toughness values [38].

The pillar splitting method was recently developed to determine fracture toughness data of especially thin films and is based on the principles of sharp indentation on a FIB milled micro-pillar [39, 40]. The load-displacement data are recorded during this indentation and the fracture toughness can easily be calculated by a relationship between pillar radius, critical load of failure regarding the first splitting and a dimensionless coefficient that includes the elastic-plastic properties. Besides the relative simple pillar design there is no necessity to measure crack length and crack geometry after testing, being a main advantage of the pillar splitting method compared to VIF. Therefore, it can be suggested that this method allows a new experimental direction of local characterization for battery materials. A recent study evaluated the fracture toughness of Al-doped LLZO, with relative density of 93% and grain size of 100 µm, using micro-pillar splitting method on single grains and yielded a value of 0.99 ± 0.05 $MPa \cdot m^{0.5}$ being, in fact, comparable to the global toughness value of 1.19 ± 0.13 $MPa \cdot m^{0.5}$ derived via VIF in the same study [32].

However, it is necessary to further extend this approach to the investigation of contribution of grain boundaries to the mechanical properties of LLZO excluding the contribution of the density, which is missing in the literature to the best of our knowledge. Therefore, the present work focuses on the mechanical properties evaluation of LLZO electrolyte aiming to verify the usage and limitations of conventional indentation and micro-pillar methods characterizing the fracture toughness for a material with different grain sizes.

2. Experimental

2.1. Synthesis of $Li_{6.6}La_3Zr_{1.6}Ta_{0.4}O_{12}$ precursor powders

LLZO precursor powders with a nominal composition of $Li_{6.6}La_3Zr_{1.6}Ta_{0.4}O_{12}$ were synthesized following conventional solid-state synthesis and solution-assisted solid-state synthesis methods to obtain powders with different morphologies with larger (≈5 µm, precursor LG) and nano-sized particles (precursor SG), respectively. Synthesis protocols are discussed in detail in the literature [42] [43] and are only briefly summarized below.

Solid state synthesis. In the solid state synthesis procedure the starting reagents LiOH (Merck, 98%), La_2O_3 (Merck, 99.9%, dried at 900°C for 10 h), ZrO_2 (Treibacher, 99.5%), Ta_2O_5

(Inframat, 99.95%) and 5 mol% aluminum (III) oxide Al_2O_3 (99.9 %, Inframat Corp., USA) were mixed in stoichiometric amounts with 20% molar excess of LiOH. A motor grinder (Retsch RM 200) with a tungsten carbide crucible and pestle was used for dry mixing the prepared powder for 1 h with a rotational speed of 100 rpm. Then, the powder was pressed in pellets and calcined for 20 h at 850°C and subsequently twice for 10 h at 1000°C. Grinding and pressing were repeated between the calcination steps.

Solution assisted solid state synthesis. In the solution assisted solid state synthesis procedure stoichiometric amounts of lanthanum nitrate hexahydrate ($La(NO_3)_3 \cdot 6H_2O$, 99.9%, Alfa Aesar), zirconium (IV) oxonitrate hydrate ($Zr(ONO_3)_2 \cdot xH_2O$, Sigma Aldrich), lithium nitrate ($LiNO_3$, 99.9%, Merk, 20% molar excess) and 5 mol% aluminum nitrate nonahydrate ($Al(NO_3)_3 \cdot 9H_2O$, 99.997%, Sigma Aldrich) were dissolved in distilled water. The solution of tantalum (V) ethoxide ($Ta(OC_2H_5)_5$, 99.9%, Strem Chemicals) in ethanol (C_2H_5OH, anhydrous 99.9 %, Sigma Aldrich) with addition of diethanolamine as chelating agent ($HN(CH_2CH_2OH)_2$ 99%, Sigma Aldrich) was added dropwise to the metal salt solution upon stirring on a magnetic stirrer. The reaction mixture was dried at 80°C overnight and calcined at 450°C for 2 hours and at 750°C for 2 hours. Aluminum sources were added as sintering additives in the both synthesis procedures.

2.2. Sintering

To obtain dense LLZO samples with larger (LG) and smaller grains (SG) from the LLZO precursors with different morphologies and the same density, a hot pressing technique was applied. The calcined powders were thoroughly ground in agate mortar and finally pelletized in a cold uniaxial press at 250 MPa. The green bodies were then hot pressed using the FCT HP W

100 system with a maximum uniaxial compaction pressure of 50 MPa for 3.5 hours (heating and cooling rate: 10°C·min^{-1}) under nitrogen atmosphere at 1150°C for the precursor LG and at 1070°C for the precursor SG. Sintered pellets were sliced into ~0.65 mm thick slices by using a diamond saw and 100% ethanol was used for rinsing during the cutting.

2.3. Characterization

The hot pressed LLZO samples were characterized regarding their phase purity and structure using X-ray diffraction (XRD) by a Bruker D4 diffractometer equipped with a Lynx-eye detector adopting a parallel geometry (reflection mode) and using Cu K$\alpha_{1,2}$-radiation (λ = 1.54184 Å). XRD data were collected at room temperature via the 10X detector adopting a step size of (2θ) = 0.02° and a counting time of 2 s per step, leading to a total counting time of about 3 hours. The relative densities of the samples were determined by the Archimedes method using water as the liquid media.

For microstructural investigations, samples were mirror-polished by SiC sandpapers up to 4000 grit and thermally etched at 1000°C for 20 min in air. Images were taken using a scanning electron microscopy (SEM) (TM 3000 tabletop microscope, Hitachi).

Inductively coupled plasma optical emission spectroscopy (ICP-OES) (Thermo Elemental, IRIS Intrepid) was used to determine the stoichiometry of the hot pressed LLZO pellets. For this 50 mg of ground in a mortar LLZO samples were dissolved in a solution of 2 g of ammonium sulfate/4 mL H_2SO_4 until the powder was complete dissolved. Then, the solution was diluted to 50 mL by using distilled water for the ICP-OES analysis. The experimental error for the ICP-OES analysis is ±3% of the detected concentration.

The conductivity of the hot pressed LLZO pellets was analysed by electrochemical ac impedance spectroscopy (IS) at 25°C using a BioLogic VMP-300 multipotentiostat, combined with a climate chamber (Vötsch Industrietechnik VT 4002EMC) and Swagelok cells. Au was sputtered on the LLZO samples as the blocking electrodes. In order to avoid the reaction of LLZO with moist air, the half-cells were assembled in an Ar-filled glovebox. The measured frequency was varied from 7 MHz to 1 Hz with an electrical field perturbation of 20 $\mathrm{mV\ mm^{-1}}$. The obtained data were analysed by a ZView software.

2.4. Mechanical properties

Hardness (*H*) and elastic modulus (*E*) of the hot-pressed samples were determined using a nanoindenter Nanotest Xtreme (MicroMaterials) equipped with a fixed objective microscope (magnification of 20×). Polished surfaces were indented with a diamond Berkovich tip and properties were measured using multiple loading cycles with increasing load, from 1 mN up to 50 mN and 20 cycles of loading and unloading down to 20%. The holding time of 1 second at the maximum load was applied and a grid of 5 × 5 equally spaced indents was performed on the surface leading results to an average value of 25 indentations. The *H* and *E* were evaluated from indentation load-displacement curve according to Oliver and Pharr procedure [44, 45]. To obtain the elastic modulus the unloading portion of the load - depth curve is analyzed and *H* and *E* are derived from [46]:

$$H = \frac{P_{max}}{A} \tag{1}$$

where P_{max} is the maximum applied load, A is the projection area of contact and is calculated from the geometry of the indenter and stiffness of the contact. Based on the slope of the unloading curve, dF/dh, the elastic modulus of the tested sample E_s can be calculated using the following equations:

$$E_r = \frac{1}{2} \cdot \frac{dF}{dh} \cdot \sqrt{\frac{\pi}{A}} \tag{2}$$

$$\frac{1}{E_r} = \frac{1-\vartheta_s^2}{E_s} + \frac{1-\vartheta_i^2}{E_i} \tag{3}$$

where the E_r is the reduced elastic modulus, A the contact area, ν_s the Poisson's ratio of the sample, E_i and ν_i the elastic modulus and Poisson's ratio of the indenter tip, respectively. In this work, a Poisson's ratio, ν_i = 0.07, and Young's modulus, E_i = 1141 GPa, for the diamond indenter tip were adopted.

The fracture toughness values were obtained via conventional Vickers indentation method (VIF) and via micro-pillar splitting test utilizing a Berkovich tip indenter. The Berkovich indenter was adopted for pillar splitting due to its sharp edge leading to a reproducible load for pillar fracture [39, 47, 48]. For VIF, the surface was prepared as described above, and the applied loads were 0.5 N, 1 N and 3 N for 3 to 5 imprints (Fischer HC100) to induce the cracks formation. The crack lengths were determined from SEM images and the K_{IC} for the observed Palmqvist crack system was calculated using [49]:

$$K_{IC} = 0.018 \cdot H \cdot a^{0.5} \cdot \left(\frac{E}{H}\right)^{0.4} \cdot \left(\frac{l}{a}\right)^{-0.5} \tag{4}$$

where H is the hardness, E the elastic modulus, a the half diagonal of the Vickers imprint and l the crack length as measured from the edge of the imprint. This equation (4) has been widely used for fracture toughness evaluation for ceramic materials [50, 51] especially the LLZO materials [36], and in the work [36] it was proved that this equation can be used successfully measuring the fracture toughness.

For the micro-pillar splitting tests, pillars of 5 and 10 µm diameter were milled using a focus ion beam machine (FIB dual ion beam scanning electron microscope FIB-SEMs; Zeiss Auriga) operated at 30 kV and 2 - 16 nA. The pillar diameter was varied since a recent publication indicated a pillar size effect, i.e. a significant increase can occur in the apparent toughness for smaller pillars sizes due to ion surface interaction [52]. SEM micrographs of the pillars are presented in Figure 1. The aspect ratio (*h*/*D*), where *h* is the pillar height and *D* is the top diameter, was fixed to ~ 1 in order to avoid any effects of potential residual stress in the top surface of the pillar [39, 40]. The resulting pillar size was then measured by SEM imaging using the software AnalySIS Pro®.

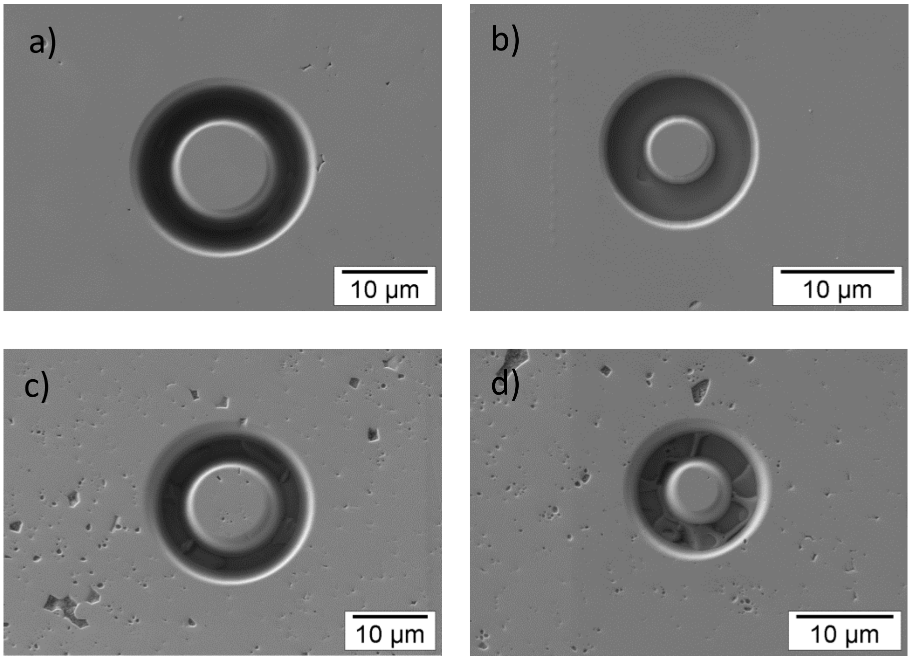

Figure 1: SEM topography of micro-pillar in hot pressed LLZO LG and SG samples before testing, a) 10 µm pillar diameter LG LLZO, b) 5 µm pillar diameter LG LLZO, c) 10 µm pillar diameter SG LLZO and d) 5 µm pillar diameter SG LLZO.

The splitting test was performed using a Nanotest Xtreme nanoindenter equipped with optical microscope (20×), the surface of the micro-pillar was scanned before indentation with imaging load of 0.002 mN and step size of 0.2 µm and the indentation placed in the center of the pillar. The load-displacement curves were recorded during the load-controlled indentation, while increasing the load to a maximum of 50 mN for 10 µm pillar diameter and 25 mN for 5 µm pillar diameter, while loading and unloading rates of 10 mN/s were applied. The fracture toughness was then calculated using [40]:

$$K_c = \gamma \cdot \frac{P_c}{R^{3/2}} \tag{5}$$

where P_c is the critical load at splitting failure, R the pillar radius and γ a dimensionless coefficient that includes the influence of elastic-plastic properties. The coefficient γ has been evaluated for several materials via Cohesive-Zone Finite Element Modeling (CZ-FEM) [39, 40] and can be estimated by the linear relationship $\gamma = 0.0149 \cdot \left(\frac{E}{H}\right) + 0.057$ for E/H ranging from 5 to 21 [53].

3. Results and discussion

As outlined above, dense LLZO samples (99% of the theoretical density) with larger (LG) and smaller (SG) grains (D50 8.4 and 2.8µm respectively, Table 1, Figure 2 a), b)) were obtained by hot pressing of LLZO precursor powders with different morphologies. The composition

$Li_{6.6}La_3Zr_{1.6}Ta_{0.4}O_{12}$ for the both samples was confirmed by ICP-OES. 5 mol% of Al was added to the starting reagents as a sintering additive [54]. However, the concentration of Al in the hot pressed pellets appeared to be below the detection limit of ICP-OES. This can be explained by the formation of lithium aluminates during thermal treatment. The melting point of the most thermodynamically stable lithium aluminate Li_5AlO_4 is 1064°C [55], which is below the hot pressing temperature of the both specimens. Therefore, liquid lithium aluminates presumably diffused out of the samples during the hot pressing process.

Figure 2 illustrates the microstructure and corresponding XRD patterns of the hot pressed LLZO samples from the precursors synthetized via conventional solid-state synthesis (LG) and solution-assisted solid-state synthesis (SG). The XRD analysis of the sintered pellets revealed the formation of a pure cubic phase of the garnet type (space group Ia3d (230), see Figure 2 c). The total conductivity of the sintered pellets, determined by means of electrochemical impedance spectroscopy (Table 1), is in good agreement with literature values [42]. both LLZO samples ($7.8 – 8.4\times10^{-4}$ S/cm) possess better conductivity than some typical solid electrolytes for lithium ion battery like LIPON (3.3×10^{-6} S/cm) [56], LISICON (~ 10^{-6} S/cm) [57-59].

a)

c)

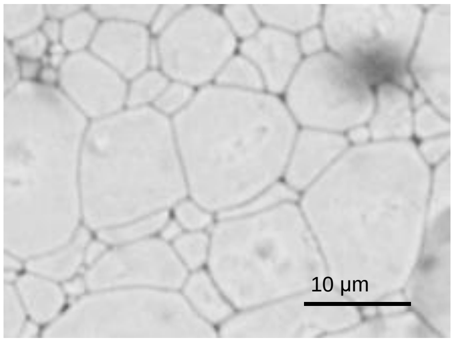

b)

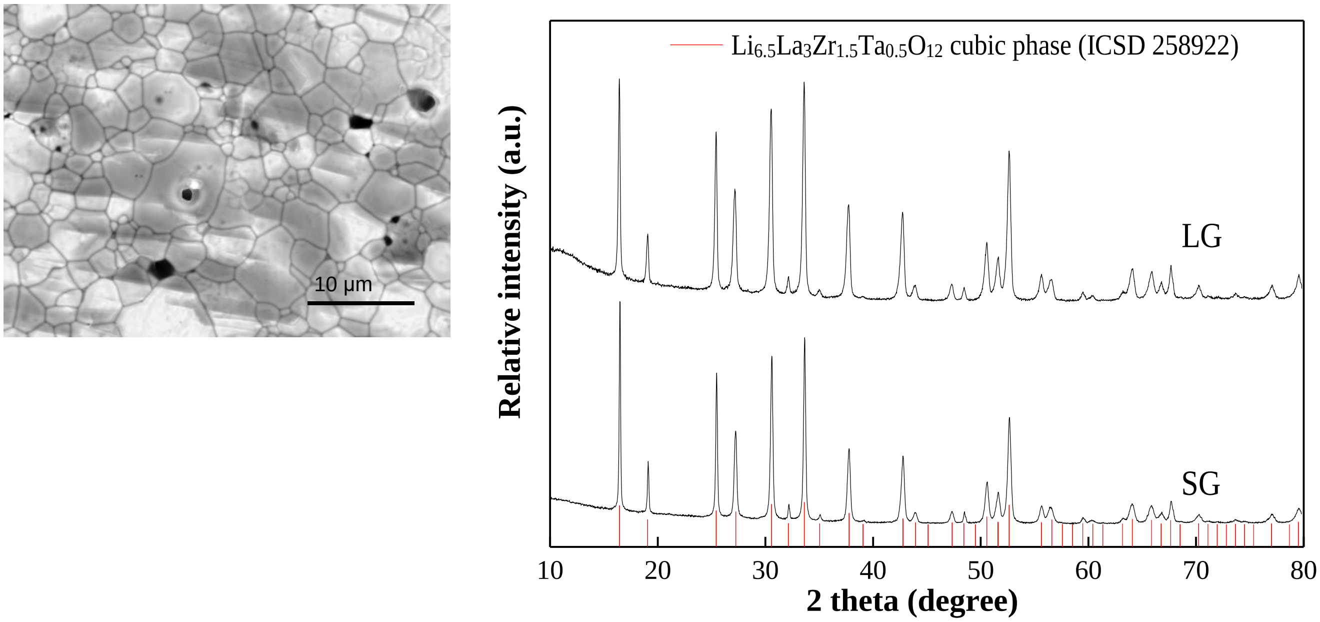

Figure 2: SEM micrographs of a LG (a) and SG (b) LLZO samples with the corresponding XRD patterns and reference reflexes for cubic $Li_{6.5}La_3Zr_{1.5}Ta_{0.5}O_{12}$ (c) **[60]**.

Table 1: Summary of microstructural and electrochemical properties of LLZO

Specimen	**Composition***	**Relative Density (%)**	**D50 (µm)**	**Conductivity $\sigma_{25°C}$ ($S{\cdot}cm^{-1}$)**
LLZO-LG	$Li_{6.6}La_3Zr_{1.6}Ta_{0.4}O_{12}$	≥ 99	8.4	$8.4{\cdot}10^{-4}$
LLZO-SG	$Li_{6.6}La_3Zr_{1.6}Ta_{0.4}O_{12}$	≥ 99	2.8	$7.8{\cdot}10^{-4}$

*based on the ICP-OES analysis of Al-, Li-, La-, Ta- and Zr-concentrations

The average values for elastic modulus and hardness, resulting from 25 indentations for each depth, obtained from indentation testing of the LG and SG LLZO samples, as a function of depth are presented in Figure 3. Elastic modulus and hardness values are rather constant in the displacement range from ~ 300 to ~ 600 nm, a slight increase of the hardness up to around 200 µm can be related to tip rounding effects. Therefore Table 2 summarizes the values at the penetration depth of 500 nm within the stable region of constant elastic modulus and hardness values, which can be considered to correspond to the materials properties. No indentation size effect in the hardness was noticeable, since hardness values are constant for all samples once the range where tip rounding effects can be expected is exceeded.

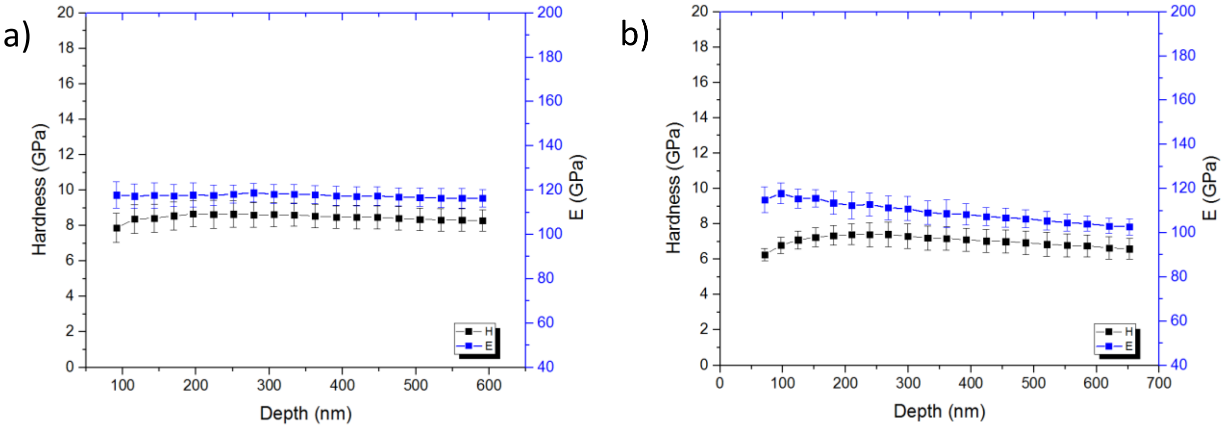

Figure 3: *H* and *E* as function of penetration depth for a) LG and b) SG LLZO samples.

Table 2: Mechanical properties of LG and SG LLZO samples.

Specimen	**Elastic Modulus *E*, (GPa)**	**Hardness *H*, (GPa)**
LLZO-LG	119 ± 5	8.2 ± 0.7
LLZO-SG	108 ± 4	7.4 ± 0.6

The elastic modulus of the LG sample appears to have a ~10% higher value in comparison to that of the SG sample. The elastic modulus is an intrinsic material property fundamentally related to the bond strength between atoms. Higher elastic modulus of the LG sample might be caused by its higher crystallinity due to the heat treatment of the precursor powder at a higher temperature for a longer time and higher hot pressing temperature. Hardness is governed by both intrinsic properties (i.e. bond strength, cohesive energy and crystal structure), and extrinsic properties, such as stress fields, defects and morphology [61]. LG LLZO sample exhibits also 10% higher value for hardness in comparison to the SG sample. Overall, it is in good agreement with the literature data for the correlation between grain sizes and hardness of ceramic materials, demonstrating that hardness commonly increases with increasing grain sizes toward single-crystal values at larger grain sizes [62].

The fracture toughness was estimated for the two specimens using Vickers indentation applying loads of 0.5 N, 1 N and 3 N. Figure 4 shows SEM images of typical Vickers indentation imprints in the hot pressed LLZO pellets after applying the different loads.

For the LG sample, the crack shape is straight (see Figure 4 a)), and the fracture toughness is independent of the applied load in the range from 0.5 to 1 N within the experimental uncertainty limits. At 3 N the formation of numerous secondary micro-cracks is observed for the both specimens. Such an effect might be related to the high local stress field at 3 N, leading to the dissipation of the indentation energy. Therefore an accurate fracture toughness calculation is not allowed at this load. The cracks are deflected at the grain boundaries and stop at residual pores for the SG sample (see Figure 4 b)). With a clear look in Fig. 5 it can be found that in smaller grain sample the crack propagates intergranularly and for larger grain sample the crack propagates mainly transgranularly as expected that for a cubic material the transgranular fracture may occur for larger grain sizes.

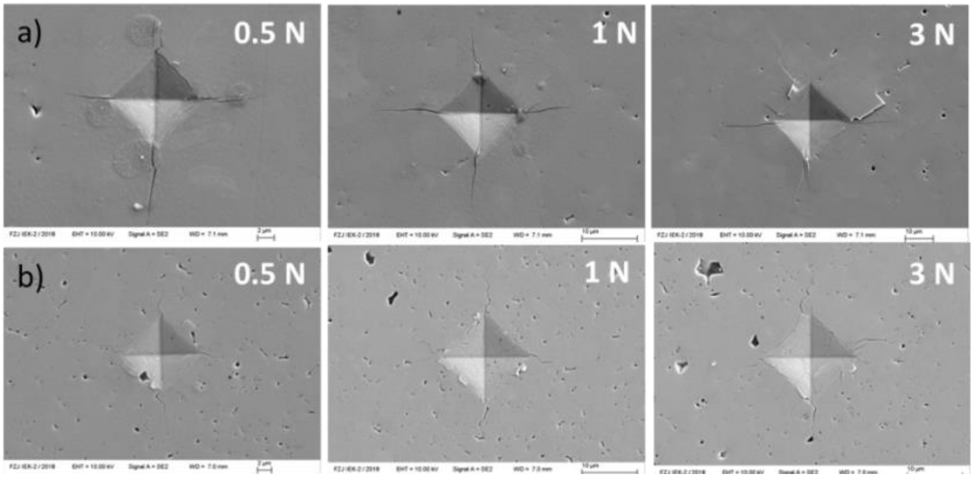

Figure 4: SEM micrographs of Vickers indentation imprints after loading to 0.5 N, 1 N and 3 N for a) LG LLZO, b) SG LLZO.

The average crack lengths (l), the ratio l/a derived from the SEM images and calculated K_{IC} values are compiled in Table 3. Based on the crack length (l) and half diagonal (a) ratio, the Palmqvist crack system was selected for calculation (criterion $0.25 \leq l/a \leq 2.5$) and equation (4) was used to calculate K_{IC}.

Table 3: Vickers indentation fracture toughness results for LG and SG LLZO samples.

Specimen	**Load (N)**	**Average crack length l (μm)**	**l/a**	**K_{IC} (MPa·m$^{0.5}$)**
LG LLZO	0.5	6.4 ± 0.5	1.2	0.93 ± 0.05
	1	10.0 ± 0.7	1.3	1.07 ± 0.05
	3	20.0 ± 1.5	1.5	-
SG LLZO	0.5	5.0 ± 0.5	0.9	0.95 ± 0.05
	1	7.4 ± 0.5	1.0	1.10 ± 0.05
	3	14.5 ± 0.5	1.3	-

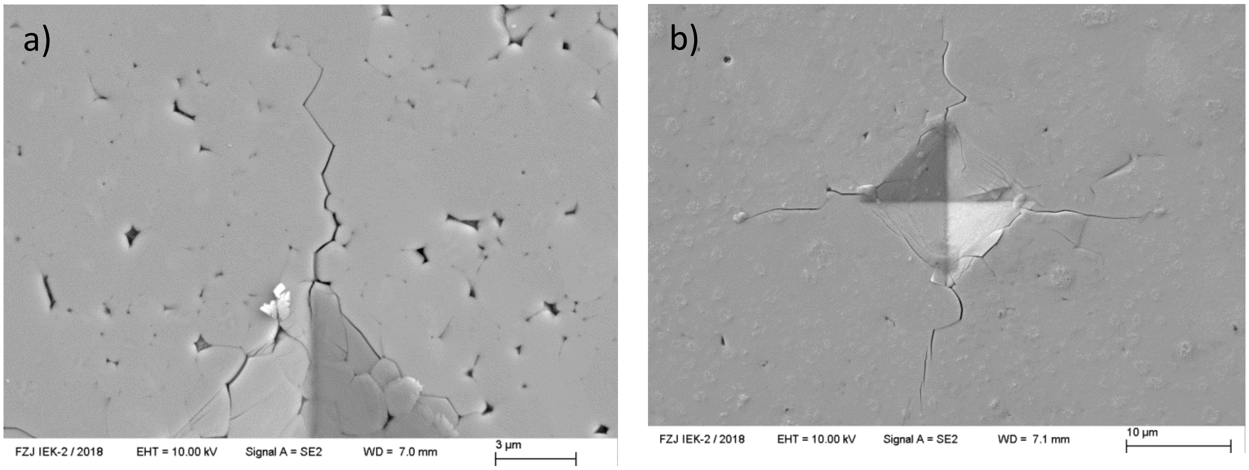

Figure 5: Cracks after indentation load of 1 N, along the grain boundary for a) SG LLZO, b) LG LLZO samples.

The micro-pillar testing was carried out for the small and large grain size LLZO samples. Figure 6 presents the load-displacement curves of micro-pillars and SEM images of micro-pillars after testing. Figure 6 a) and b) show the load-displacement curves for pillars with 5 and 10 µm diameters of LG LLZO and Figure 6 c) and d) show the load-displacement curves for pillars with 5 and 10 µm diameter of SG LLZO sample.

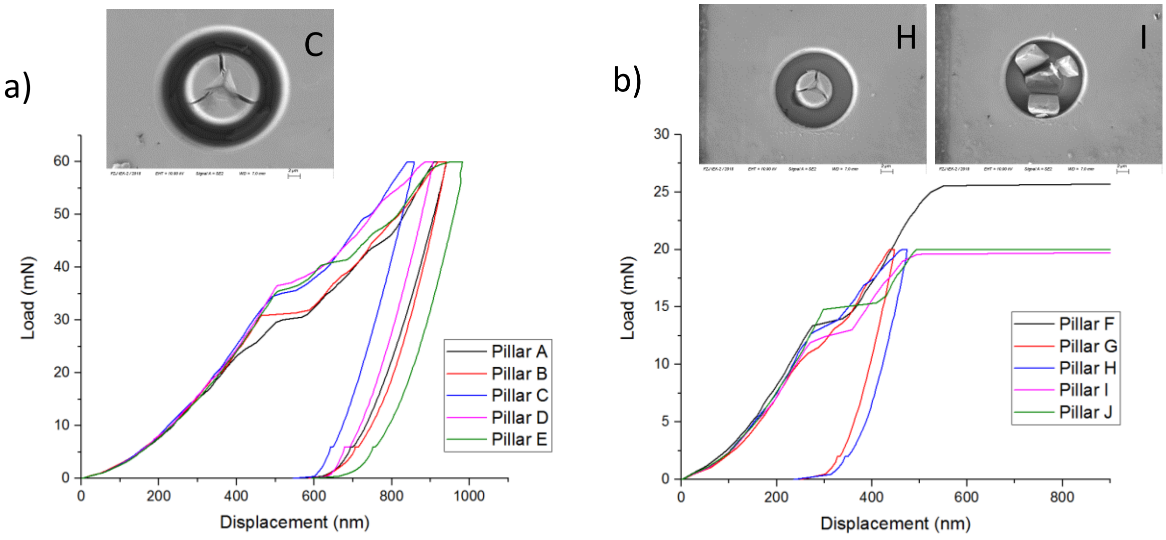

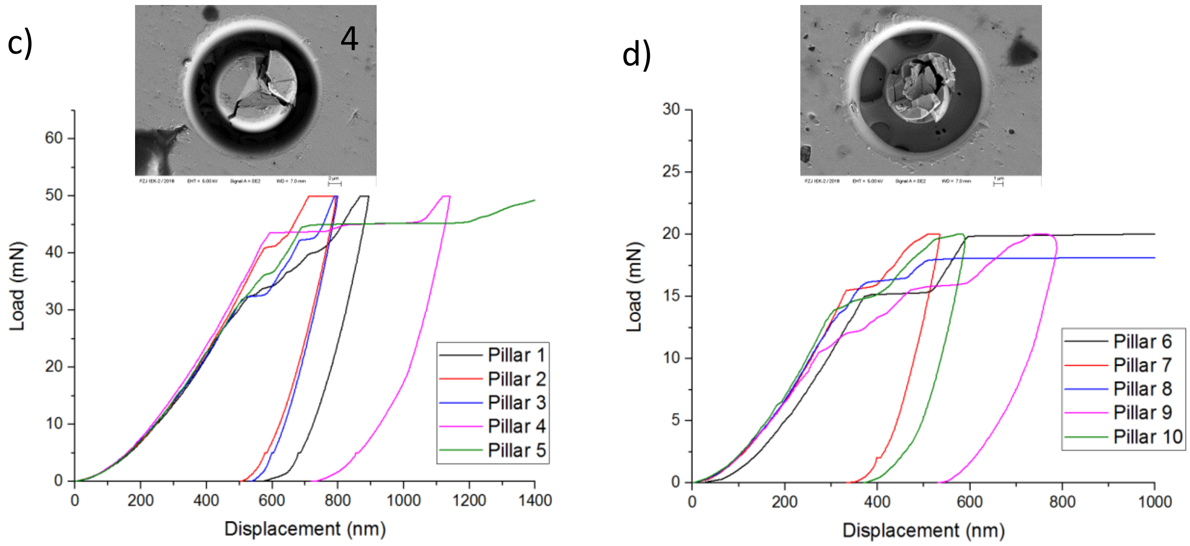

Figure 6: Load-displacement curves of micro-pillar indentation splitting tests and SEM front view of pillars after testing: a) LG pillars A to E with ~10 µm diameter, b) LG pillars F to J with ~5 µm diameter, c) SG pillars 1 to 5 with ~10 µm diameter, d) SG pillars 6 to 10 with ~5 µm diameter.

Young's modulus and hardness reported in the present work were used to derive the dimensionless coefficient γ (~0.27) for micro-pillar splitting fracture toughness calculations, the resulting values are compiled in Table 4.

Table 4: Experimental results of pillar splitting tests.

Specimen	**Number of pillars**	**Pillar radius, *R* (µm)**	**Critical load of failure, P_c (mN)**	**Fracture Toughness, K_{IC} (MPa·m$^{0.5}$)**
LG LLZO	5	2.45 ± 0.04	12.9 ± 1.2	0.91 ± 0.09
	5	5.03 ± 0.06	33.4 ± 2.5	0.80 ± 0.05
SG LLZO	5	2.31 ± 0.05	13.75 ± 1.7	1.06 ± 0.15
	5	4.78 ± 0.10	37.0 ± 4.5	0.96 ± 0.12

For LG samples, the average pillar radius was 2.45 ± 0.04 μm and the associated fracture toughness value was 0.91 ± 0.09 MPa·m$^{0.5}$, very close to the K_{IC} of 0.80 ± 0.05 MPa·m$^{0.5}$ for the average pillar radius of 5.03 ± 0.06 μm. Individual values can be found in appendix. Considering that the grain size ranged was 2.8 to 8.4 μm, pillars with 2.5 and 5 μm radii were fabricated preferentially within single grains. Hence the obtained values can be associated with the intrinsic fracture toughness of LLZO. Compared with literature, the single crystal fracture toughness of similar dopant level LLZO via micro-pillar method for a pillar diameter of 10 μm has been reported as 0.99 ± 0.05 MPa·m$^{0.5}$ [32]; being in similar range as the one obtained in this work.

For the SG sample, the average pillar radii were 2.31 ± 0.05 μm and 4.78 ± 0.10 μm, respectively, and the associated K_{IC} values 1.06 ± 0.15 MPa·m$^{0.5}$ and 0.96 ± 0.12 MPa·m$^{0.5}$, respectively. The average grains size was 2-3 μm; therefore the fracture toughness results in this case can be ascribed to a polycrystalline material considering inherent grain boundary effects.

Comparing the micro-pillars with ~2.5 μm and ~5 μm radius, in both cases for the apparent single crystal and polycrystalline material, pillars with smaller size show a tendency towards higher fracture toughness values when compared to pillars with larger diameter. The increase in K_{IC} for smaller pillars might indicate that gallium damage can influence the fracture toughness, particularly for pillars with smaller diameters similar as reported in literature, hence considering a conservative approach the values for the 10 μm pillar appear to be representative of the materials behavior. It was recently reported that K_{IC} significantly increased with decreasing diameter due to FIB damage on Si pillars, even though it has been suggested that this geometry is insensitive to FIB damage since the crack nucleates inside the pillar, far from the damaged free surface [39, 52]. In general it can also be possible that the grain boundaries absorb the crack energy to help the pillar sustain with higher load, which can be seen in Fig. 8 a). Especially for the comparison of the larger and smaller size of pillars, the larger pillar contains more grain boundaries, could hence lead to a higher fracture toughness, which appears to be an additional effect explaining the differences of the LG and SG values.

In order to investigate the influence of Ga-ion damage on the pillar, an EDS study was performed for one of the pillars with 5 µm diameter; the results are shown in Figure 7. It can be seen that Ga is concentrated on the edges of the pillar (brighter area), which might influence pillars with smaller diameter to some extent, since the distance between the center, where the indentation is imprinted, and the edges is shorter. According to Lauener et al., the influence of FIB damage diminishes and becomes negligibility for pillar diameters of around 10 µm and larger [52], where the small difference obtained for the results of the 5 and 10 µm pillars indicates that the values obtained for the 10 µm pillars are already representative for the materials property.

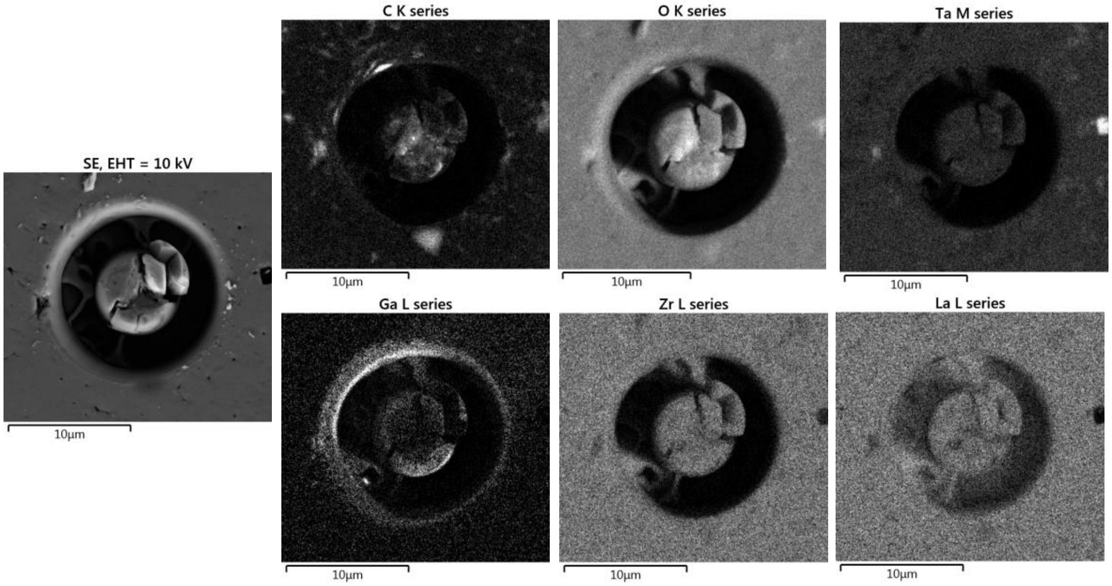

Figure 7: EDS of pillar 9 (5 µm diameter) after testing, sample SG LLZO.

Additionally, in order to investigate the crack characteristic after testing in more details, pillars H and 5 were chosen as matter of exercise and were submitted to a cross-section FIB cut, see Figure 8, even though the micro-pillar splitting method evaluation does not require any crack measurement. Looking at Figure 8 a), the crack trajectory was rather straight and did not encounter any structural defects, whereas for the pillar in Figure 8 b) the crack trajectory deviates with a preferential path along the grain boundaries.

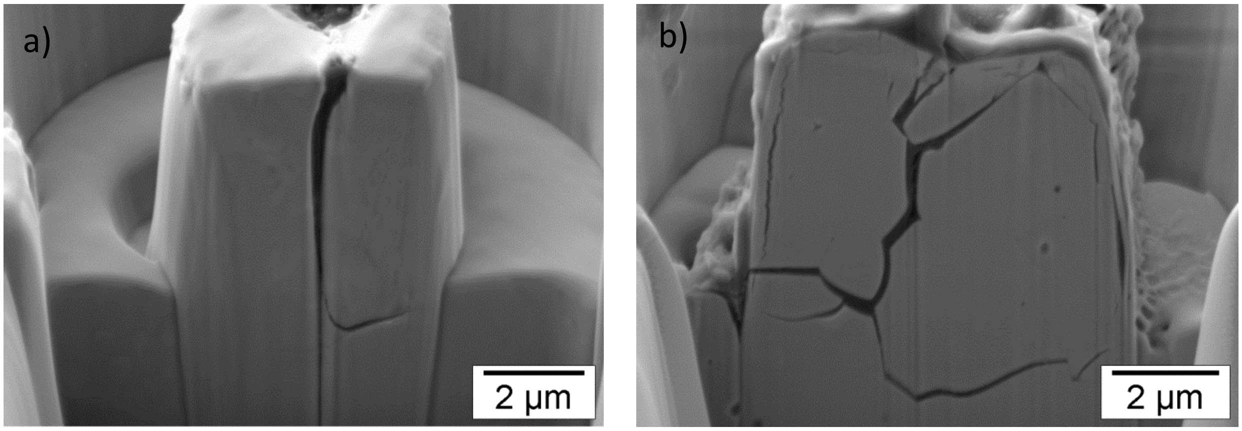

Figure 8: SEM micrographs of cross-sectional FIB cut of pillar with 5 μm diameter, a) pillar H of the LG and b) pillar 5 of SG LLZO samples.

The results for the average fracture toughness of the polycrystalline LLZO sample with small grains (SG), obtained by the two different methods for K_{IC} determination (micro-pillar and VIF) are in a very good agreement: ~1.02 $MPa \cdot m^{0.5}$ and 0.98 $MPa \cdot m^{0.5}$ respectively. The fracture toughness values obtained in this work are in the same range as those reported in the literature (0.86 – 1.63 $MPa \cdot m^{0.5}$ for cubic dense LLZO with mean grain size of ~ 5 μm [36]). For a similar material, Al-substituted cubic garnet $Li_{6.19}Al_{0.27}La_3Zr_2O_{12}$ produced by cold pressing with 98% density and grain size of ~3 μm, the reported fracture toughness is 0.97 ± 0.1 $MPa \cdot m^{0.5}$ [35], which is also in good agreement with the values reported here. In addition, it has been reported that K_{IC} is independent of grain size for cubic oxides at room temperature in the grain size range from 10 to 150 μm [63, 64]. Therefore, for the grain size range investigated in the present work, the fracture toughness obtained via micro-pillar splitting method is comparable to conventional VIF.

4. Conclusions

This work presented the mechanical properties of dense $Li_{6.6}La_3Ta_{0.4}Zr_{1.6}O_{12}$ samples, as well as the usage assessment of micro-pillar splitting method for fracture toughness estimation for LLZO samples with larger and smaller grains comparing to conventional indentation test method.

- Mechanical properties of dense $Li_{6.6}La_3Ta_{0.4}Zr_{1.6}O_{12}$ samples with larger and smaller grains were evaluated in this work. The LLZO sample with larger grains has ~10% higher elastic modulus and ~10% higher hardness values compared to those of the sample with smaller grains. The higher hardness values for the sample with larger grains correlates well with the literature data, demonstrating that hardness of ceramic materials commonly increases with increasing grain sizes toward single-crystal values at larger grain sizes.
- The fracture toughness of the LLZO materials, determined by a combination of Vickers indentation and a pillar splitting methods, are a good agreement within the experimental uncertainty limits, yielding an average value of ~ 1 $MPa \cdot m^{0.5}$ for the both samples.
- According to the results of the Vickers indentation tests, the fracture toughness of LLZO samples is apparently independent of the grain size. The fracture toughness determined by the pillar splitting test is slightly higher of the smaller grain sample than the larger grain sample, whereas for both samples the values of the pillars with 10 µm diameters are higher than that of 5 µm diameters pillars. This reveals a positive effect of the grain boundaries on the fracture toughness, which is crucial for application and a negative effect on the conductivity.

Overall, as the material is a cubic ceramic, there is no reinforcement and the ceramic remains brittle, whatever the grain size. Since the grain boundary performs a negative effect on the conductivity, the investigation indicates the material needs to be carefully engineered towards achieving optimal properties for the application (e.g. in case of being used as separator or mixed cathode) and it has to be emphasized that the used micro-pillar method is suitable for determining in particular the local values aiding such engineering.

Acknowledgment

This work was supported by the National Council for Scientific and Technological Development (CNPq) of Brazil, The Federal Ministry of Education and Research of Germany (project MEET Hi-End II, project number 03XP0084A), the China Scholarship Council (CSC) of China and German Academic Exchange Service (DAAD). The authors are grateful to Dr. E. Wessel for SEM characterization, Ms. D. Esser for FIB preparation and Prof. L. Singheiser for his support.

References

[1] Y. Arinicheva, M. Wolff, S. Lobe, C. Dellen, D. Fattakhova-Rohlfing, O. Guillon, D. Böhme, F. Zoller, R. Schmuch, J. Li, M. Winter, E. Adamc, V. Pralong, Ceramics for electrochemical storage, in: O. Guillon (Ed.) Advanced Ceramics for Energy Conversion and Storage, Elsevier Ltd., 2020, pp. 549-709.
[2] P. Bieker, M. Winter, Chemie in unserer Zeit, 50 (2016) 172-186.
[3] T. Placke, R. Kloepsch, S. Dühnen, M. Winter, Journal of Solid State Electrochemistry, 21 (2017) 1939-1964.
[4] V. Thangadurai, S. Narayanan, D. Pinzaru, Chem Soc Rev, 43 (2014) 4714-4727.
[5] R. Murugan, V. Thangadurai, W. Weppner, Angewandte Chemie International Edition, 46 (2007) 7778-7781.
[6] J. Wolfenstine, J.L. Allen, J. Read, J. Sakamoto, Journal of Materials Science, 48 (2013) 5846-5851.
[7] J. Awaka, N. Kijima, H. Hayakawa, J. Akimoto, Journal of Solid State Chemistry, 182 (2009) 2046-2052.
[8] M. Huang, A. Dumon, C.-W. Nan, Electrochemistry Communications, 21 (2012) 62-64.
[9] Y. Shimonishi, A. Toda, T. Zhang, A. Hirano, N. Imanishi, O. Yamamoto, Y. Takeda, Solid State Ionics, 183 (2011) 48-53.
[10] T. Thompson, A. Sharafi, M.D. Johannes, A. Huq, J.L. Allen, J. Wolfenstine, J. Sakamoto, Advanced Energy Materials, 5 (2015) 1500096.
[11] T. Thompson, J. Wolfenstine, J.L. Allen, M. Johannes, A. Huq, I.N. David, J. Sakamoto, J. Mater. Chem. A, 2 (2014) 13431-13436.
[12] D.O. Shin, K. Oh, K.M. Kim, K.Y. Park, B. Lee, Y.G. Lee, K. Kang, Sci Rep, 5 (2015) 18053.
[13] M. Matsui, K. Takahashi, K. Sakamoto, A. Hirano, Y. Takeda, O. Yamamoto, N. Imanishi, Dalton Transactions, 43 (2014) 1019-1024.
[14] A. Sharafi, C.G. Haslam, R.D. Kerns, J. Wolfenstine, J. Sakamoto, J. Mater. Chem. A, 5 (2017) 21491-21504.
[15] G. Yan, S. Yu, J.F. Nonemacher, H. Tempel, H. Kungl, J. Malzbender, R.-A. Eichel, M. Krüger, Ceram Int, 45 (2019) 14697-14703.
[16] G. Yan, J.F. Nonemacher, H. Zheng, M. Finsterbusch, J. Malzbender, M. Krüger, Journal of materials science, 54 (2019) 5671-5681.
[17] X. Hu, G. Yan, X. Cheng, J. Malzbender, W. Qiang, B. Huang, J Am Ceram Soc, 102 (2019) 1953-1960.
[18] J.F. Nonemacher, C. Hüter, H. Zheng, J. Malzbender, M. Krüger, R. Spatschek, M. Finsterbusch, Solid State Ionics, 321 (2018) 126-134.

[19] G. Yan, S. Yu, W. Yang, X. Li, H. Tempel, H. Kungl, R.-A. Eichel, M. Krüger, J. Malzbender, J Power Sources, 437 (2019) 226940.
[20] G. Bucci, T. Swamy, S. Bishop, B.W. Sheldon, Y.-M. Chiang, W.C. Carter, Journal of The Electrochemical Society, 164 (2017) A645-A654.
[21] H. Tavassol, E.M. Jones, N.R. Sottos, A.A. Gewirth, Nat Mater, 15 (2016) 1182-1187.
[22] K. Kerman, A. Luntz, V. Viswanathan, Y.-M. Chiang, Z. Chen, J Electrochem Soc, 164 (2017) A1731-A1744.
[23] P.G. Balakrishnan, R. Ramesh, T. Prem Kumar, Journal of Power Sources, 155 (2006) 401-414.
[24] P. Verma, P. Maire, P. Novák, Electrochim Acta, 55 (2010) 6332-6341.
[25] Y. Ren, Y. Shen, Y. Lin, C.-W. Nan, Electrochemistry Communications, 57 (2015) 27-30.
[26] P. Wang, W. Qu, W.L. Song, H. Chen, R. Chen, D. Fang, Advanced Functional Materials, (2019).
[27] E.J. Cheng, A. Sharafi, J. Sakamoto, Electrochimica Acta, 223 (2017) 85-91.
[28] R. Raj, J. Wolfenstine, Journal of Power Sources, 343 (2017) 119-126.
[29] M.W. Barsoum, McGraw Hill, (1997).
[30] Y. Chiang, D. Birnie III, W. Kingery, Physical Ceramics: Principles for Ceramic Science and Engineering New York, John Wiley & Sons, (1997) 351-513.
[31] R. DAVIDGE, in, Cambridge Univ. Press, 1979.
[32] A.-N. Wang, J.F. Nonemacher, G. Yan, M. Finsterbusch, J. Malzbender, M. Krüger, Journal of the European Ceramic Society, 38 (2018) 3201-3209.
[33] J.E. Ni, E.D. Case, J.S. Sakamoto, E. Rangasamy, J.B. Wolfenstine, Journal of Materials Science, 47 (2012) 7978-7985.
[34] S. Yu, R.D. Schmidt, R. Garcia-Mendez, E. Herbert, N.J. Dudney, J.B. Wolfenstine, J. Sakamoto, D.J. Siegel, Chemistry of Materials, 28 (2015) 197-206.
[35] Y. Kim, H. Jo, J.L. Allen, H. Choe, J. Wolfenstine, J. Sakamoto, G. Pharr, Journal of the American Ceramic Society, 99 (2016) 1367-1374.
[36] J. Wolfenstine, H. Jo, Y.-H. Cho, I.N. David, P. Askeland, E.D. Case, H. Kim, H. Choe, J. Sakamoto, Mater Lett, 96 (2013) 117-120.
[37] X. Huang, C. Liu, Y. Lu, T. Xiu, J. Jin, M.E. Badding, Z. Wen, Journal of Power Sources, 382 (2018) 190-197.
[38] A. Sharafi, C.G. Haslam, R.D. Kerns, J. Wolfenstine, J. Sakamoto, J Mater Chem A, 5 (2017) 21491-21504.
[39] M. Sebastiani, K.E. Johanns, E.G. Herbert, G.M. Pharr, Current Opinion in Solid State and Materials Science, 19 (2015) 324-333.
[40] M. Sebastiani, K.E. Johanns, E.G. Herbert, F. Carassiti, G.M. Pharr, Philosophical Magazine, 95 (2014) 1928-1944.
[41] M.Z. Mughal, R. Moscatelli, H.-Y. Amanieu, M. Sebastiani, Scripta Materialia, 116 (2016) 62-66.
[42] C.L.R. Tsai, V.; Chandran, C. V.; Ma, Q.; Uhlenbruck, S.; Bram, M.; Heitjans, P.; Guillon, O., ACS Appl. Mater. Interfaces., 8 (2016) 10617.
[43] S.A. Yoon, N.R. Oh, A.R. Yoo, H.G. Lee, H.C. Lee, Journal of the Korean Ceramic Society, 54 (2017) 278-284.
[44] W.C. Oliver, G.M. Pharr, Journal of materials research, 7 (1992) 1564-1583.
[45] W.C. Oliver, G.M. Pharr, J Mater Res, 19 (2004) 3-20.
[46] J. Malzbender, J Eur Ceram Soc, 23 (2003) 1355-1359.
[47] M. Sebastiani, K.E. Johanns, E.G. Herbert, F. Carassiti, G.M. Pharr, Philos Mag, 95 (2015) 1928-1944.
[48] M.Z. Mughal, R. Moscatelli, H.-Y. Amanieu, M. Sebastiani, Scripta Mater., 116 (2016) 62-66.
[49] K. Niihara, R. Morena, D. Hasselman, Journal of Materials Science Letters, 1 (1982) 13-16.
[50] A. Kocjan, Z.J.J.o.t.E.C.S. Shen, 33 (2013) 3165-3176.

[51] Y.-H. Cho, J. Wolfenstine, E. Rangasamy, H. Kim, H. Choe, J. Sakamoto, Journal of Materials Science, 47 (2012) 5970-5977.
[52] C.M. Lauener, L. Petho, M. Chen, Y. Xiao, J. Michler, J.M. Wheeler, Materials & Design, 142 (2018) 340-349.
[53] B.J. Eggleton, S. Palomba, A.J.G. Lunt, G. Mohanty, T.K. Neo, J. Michler, A.M. Korsunsky, 9668 (2015) 96685S.
[54] R.-J. Chen, M. Huang, W.-Z. Huang, Y. Shen, Y.-H. Lin, C.-W. Nan, Solid State Ionics, 265 (2014) 7-12.
[55] Y. Ikeda, H. Ito, G. Matsumoto, H. Hayashi, Journal of Nuclear Science and Technology, 17 (1980) 650-653.
[56] X. Yu, J. Bates, G. Jellison, F. Hart, J Electrochem Soc, 144 (1997) 524-532.
[57] R. Kanno, M. Maruyama, J Electrochem Soc, 148 (2001) A742-A746.
[58] R. Kanno, T. Hata, Y. Kawamoto, M. Irie, Solid State Ionics, 130 (2000) 97-104.
[59] Z.Q. Liu, F.Q. Huang, J.H. Yang, B.F. Wang, J.K. Sun, Solid State Ionics, 179 (2008) 1714-1716.
[60] N.K. Hamao, K.; Kijima, N.; Akimoto, J., Journal of the Ceramic Society of Japan, 124 (2016) P6-1-P6-3.
[61] H.-Y. Chung, M.B. Weinberger, J.-M. Yang, S.H. Tolbert, R.B. Kaner, Appl. Phys. Lett., 92 (2008) 261904.
[62] R.W.W. Rice, C.C.; Borchelt, F., J. Am. Chem. Soc., 77 (1994) 2539.
[63] R.W. Rice, S.W. Freiman, P.F. Becher, Journal of the American ceramic society, 64 (1981) 345-350.
[64] R. Rice, Journal of materials science, 31 (1996) 1969-1983.

Appendix

Table A.1: Summary of micro-pillar indentation splitting test results for LG LLZO, ß ≈ 0.27.

Pillar	**Diameter (μm)**	**Radius (μm)**	**Critical load of failure, *P_c***	**K_{IC} (MPa·m$^{0.5}$)**	**Average K_{IC} (MPa·m$^{0.5}$)**
A	9.85	4.93	30.1	0.74	0.80 ± 0.05
B	10.20	5.10	30.8	0.72	
C	10.10	5.05	34.5	0.82	
D	10.02	5.01	36.4	0.88	
E	10.15	5.08	35.3	0.83	
F	4.93	2.47	13.5	0.94	0.91 ± 0.09
G	4.81	2.41	12.7	0.92	
H	5.02	2.51	10.8	0.73	
I	4.90	2.45	13.0	0.92	
J	4.85	2.43	14.5	1.04	

Table A.2: Summary of micro-pillar indentation splitting test results for SG LLZO, ß ≈ 0.27.

Pillar	**Diameter (μm)**	**Radius (μm)**	**Critical load of failure, P_c**	**K_{IC} (MPa·m$^{0.5}$)**	**Average K_{IC} (MPa·m$^{0.5}$)**
1	9.25	4.63	32.3	0.88	0.96 ± 0.12
2	9.50	4.75	40.8	1.06	
3	9.80	4.90	32.2	0.80	
4	9.52	4.76	43.5	1.13	
5	9.71	4.86	36.2	0.91	
6	4.72	2.36	15.1	1.12	1.06 ± 0.15
7	4.50	2.25	15.4	1.23	
8	4.65	2.33	13.8	1.05	
9	4.70	2.35	10.6	0.79	
10	4.50	2.25	13.9	1.11	